



Drag reduction using longitudinal vortices on a flat-back Ahmed body

T. Darabasz^{1,2} · G. Bonnavion¹ · O. Cadot³ · Y. Goraguer² · J. Borée¹

Received: 26 July 2022 / Revised: 21 October 2022 / Accepted: 16 December 2022 / Published online: 7 January 2023
© The Author(s) 2023

Abstract

The paper presents different cavity wall designs at the rear of a flat-back Ahmed body to achieve drag reduction. The wake balance is assessed using the variance of the base pressure gradient and correlated to the obtained drag reduction. Without the rear cavity, the flat-back Ahmed body is subject to a steady instability producing a strong wake imbalance in the horizontal direction. The low drag rear design consists of a 5° inclined spoiler at the bottom (referred to as a diffuser) that first provokes a vertical imbalance and a non-inclined top spoiler with central imprints that re-balance the wake. The drag reduction is 11.5%, the wake structure is observed to respect the symmetry of the body base in both lateral and vertical directions suggesting a full stabilization of the initial steady instability. Both the wake balance and the stabilization are associated with the formation of a longitudinal vortex pair initiated at the imprint edges and penetrating the recirculating area.

1 Introduction

Wake balance is a concept to reduce drag of ground vehicles having a wide recirculation area at the rear, such as minivans, sport utility vehicles or lorries. It consists in orientating the separated streamlines at the salient edges of the vehicle base to achieve the wake orientation having the lower base suction. It is generally realised by modifying the top and/or the bottom body trailing edge shape. For instance, this wake control strategy has been applied for industrial geometries by De Boer et al. (2022); Chaligné et al. (2017) to reduce drag in aligned flow condition and by Urquhart and Sebben (2022) in crosswind conditions.

For simplified ground vehicle geometries such the flat-back Ahmed or Windsor bodies, the flow orientation at the base has been investigated with small chamfers (Littlewood and Passmore 2010; Pavia et al. 2016; Perry et al. 2016), spoilers (Grandemange et al. 2013c) and boat tails (Wong and Mair 1983; Han et al. 1992). With spoilers, it is shown (Grandemange et al. 2013c) that the drag can always been minimized by a couple of angles at the top and bottom

of the base. The minimum is a compromise between a thin wake and the drag induced by the lifting surfaces introduced by the spoilers.

On a fundamental point of view, any progress to the understanding on the relationship between the global wake dynamics and the base drag using different conditions at separation is of importance. In particular, since the wake asymmetry is associated with extra drag (Haffner et al. 2020, 2021), a wake balance leading to no wake asymmetry should achieve better drag reduction. The situation is particularly challenging for flat-back bluff bodies that are known to experience a steady wake instability over a very large span of Reynolds numbers (Grandemange et al. 2012, 2013b). The steady instability produces a permanent near wake asymmetry, with an azimuthal $m=1$ dominant mode or equivalently with a planar symmetry. This asymmetry has been reported in many works, both experimental or numerical (see for instance: Grandemange et al. (2013a); Volpe et al. (2015); Evstafyeva et al. (2017); Pavia et al. (2018); Evrard et al. (2016); Dalla Longa et al. (2019); Pavia et al. (2020); Fan et al. (2020); Podvin et al. (2021)). It is sketched in Fig. 1 featuring its main characteristics in the plane of reflectional symmetry: a large steady circular recirculation close to the base, a skewed feedback flow and a mean elliptical recirculation region bounded by a highly fluctuating shear layer indicated by the little whirls. The strong flow asymmetry in this plane is responsible for a base pressure gradient along the major axis of the rectangular base oriented from the steady recirculation

✉ O. Cadot
cadot@liv.ac.uk

¹ Institut Pprime, Université de Poitiers, UPR CNRS 3346, ISAE-ENSMA, Futuroscope-Chasseneuil, Poitiers, France

² Stellantis, Route de Gisy, 78140 Vélizy-Villacoublay, France

³ School of Engineering, University of Liverpool, L69 3GH Liverpool, UK

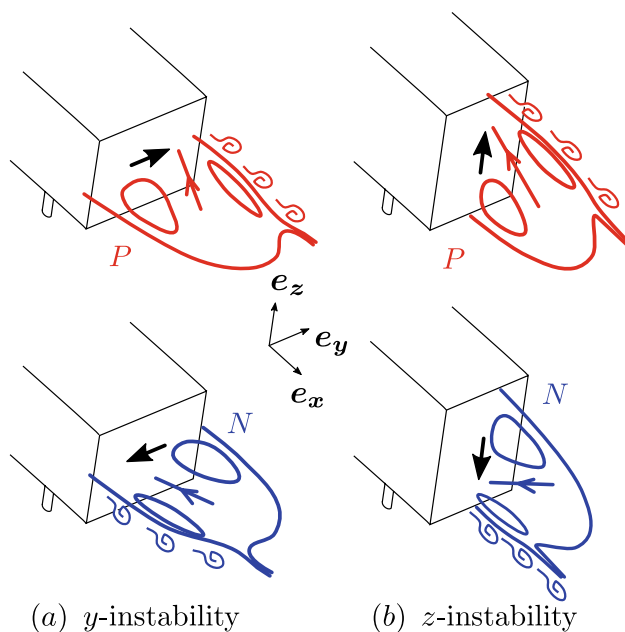


Fig. 1 Sketches of the recirculating bubbles for the y -instability **a** and z -instability **b** interpreted from the mean wake measurements of Grandemange et al. (2013a). Thick arrows display the corresponding base pressure gradients defining the P (positive) or N (negative) state depending on its sign

towards the feedback flow impingement. Due to the planar symmetry, there is no pressure gradient component in the perpendicular direction.

For a body wider than tall (Fig. 1a), the reflectional symmetry of the geometry leads to the bistable dynamics between the two possible states of the wake. A similar dynamics (Grandemange et al. 2013a; Schmidt et al. 2018; Dalla Longa et al. 2019; Fan et al. 2022) is observed for a body taller than wide (Fig. 1b), although there is no strictly speaking a reflectional symmetry because of the body supports and ground. Noticeably, the symmetry plane of the asymmetric wake can be made either horizontal or vertical with a pressure gradient of constant sign by a wide range of perturbations modifying the wake balance - namely the crosswind (Urquhart et al. 2020, 2021; Fan et al. 2022) and any modification of the underbody flow, such as the ground clearance (Grandemange et al. 2013a), perturbations (Barros et al. 2017), the wheels (Pavia and Passmore 2018; Bao et al. 2022) and the air intake (Bonnaivon et al. 2017).

There are some techniques to suppress the instability: rear cavity (Evrard et al. 2016), active pulsed jet (Li et al. 2016, 2019), active flaps (Brackston et al. 2016) and base suction (Hsu et al. 2021). However, active technologies are less likely to be implemented on real cars. Moreover, they have not been proved to be more efficient to suppress the steady instability up to now. For example, a moderate gain of 2% in base pressure is only obtained by Li et al. (2016) because

Kármán vortex shedding is emulated by the opposition control and is detrimental.

Only few works have reported on wake balance of an unstable wake. The present contribution is to propose a proof of concept study for a passive technique based on spoilers with specific design in order to achieve wake balance of stabilized wake (ie: full suppression of the steady instability in both y and z directions). The paper is organized as follows. We first describe the experimental setup in § 2, then detail the results together with discussions in § 3 and eventually conclude the work in § 4.

2 Experimental setup

2.1 Wind tunnel and model geometry

Experiments are carried out in the S620 wind-tunnel located at ISAE-ENSMA in Poitiers (France), a detailed description of which can be found for instance in Haffner et al. (2020). Briefly, it is characterized by a 2.4 m (width) and 2.6 m (height) test section; at the imposed free-stream velocity of $U_\infty = 30$ m/s, the turbulence intensity of the flow in the tunnel is about 0.5%. A raised floor composed by a flat plate is installed in the working section for placing the model. The floor is shaped with a profiled leading edge which permits the formation of a ground boundary layer of known thickness. In this case, it is about $1/6^{\text{th}}$ of the body's ground clearance used in the experiments. Its full transition to turbulence is triggered by means of a 10-mm wide strip of 250 μm -grain-sized carborundum just after the elliptic leading edge in order to fix the transition point. An reclining flap at an upwards angle of 1° ends the raised floor in order to compensate for the lift and the streamwise pressure gradient generated by the whole set-up.

The paper investigates geometrical variations about a reference body (R) depicted in Fig. 2. Its dimensions are $L = 994$ mm, $W = 350$ mm, $H = 298$ mm (base aspect ratio $\frac{W}{H} = 1.174$). The Reynolds number based on the body height is $\text{Re} = \frac{U_\infty H}{\nu} \approx 6 \times 10^5$, where ν is the kinematic viscosity of air. The forebody and supports are identical to those used in the previous work of Bonnaivon and Cadot (2019) except that for the present experiments, turbulators are installed just upstream the four rounded upstream edges to ensure the complete transition of boundary layers in order to reduce the forebody separated bubbles. The 250 μm thickness of the turbulators has been deduced from the displacement boundary layer thickness at this location computed with a RANS simulation. Viscous coating visualisation has confirmed the suppression of the separated bubbles. The ground clearance and the pitch angle of the body are respectively fixed to $G = 50$ mm = $0.168H$ and $\alpha = 0^\circ$.

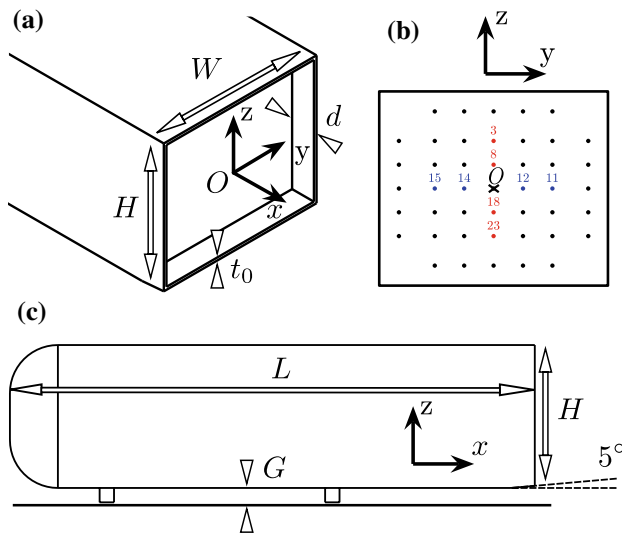


Fig. 2 Geometry of the reference body (R). Base equipped with a rear cavity **a**, the origin of the coordinates system is located at the centre of the base. Side view of the model **b** and base **c** in the plane $x = 0$ showing the location of the 45 pressure taps, those highlighted with red (resp. blue) color are used to compute the vertical (resp. horizontal) component of the base pressure gradient (see text)

The base of the reference body shown in Fig. 2a is equipped with four plain walls, which are $t_0 = 6$ mm thick and $d = 50$ mm wide, forming a cavity of depth $d = 0.168H$. As shown by Evrard et al. (2016), such a cavity depth results in an attenuation of the steady wake instability, but not to its total suppression.

The bottom cavity wall of the reference geometry is inclined with a 5° angle as shown in Fig. 2b. The reason for this angle is to suppress the lateral bistable dynamics of the wake naturally developed by the square back geometry (Fig. 1a) that is actually not observed for real vehicles (Bonnavion et al. 2017). As shown by Bonnavion and Cadot (2019), 5° is their smallest angle to fix the wake asymmetry in the vertical direction (Fig. 8). The resulting near wake develops a permanent positive base pressure gradient as illustrated in Fig. 1b,top. While it suppresses the bistable dynamics, it nevertheless does not remove the steady wake instability. A similar wake control was also employed for the Windsor body in Luckhurst et al. (2019) but with an angle of 12° .

2.2 Top cavity wall designs

In addition to the top plain cavity walls shown in Fig. 2b, three other cavity walls at the top with different geometrical designs are considered. The basic pattern depicted in Fig. 3a is either a through or a non through square $\ell \times \ell$ hole at the trailing edge. Designs with non through-holes will be referred to as imprints

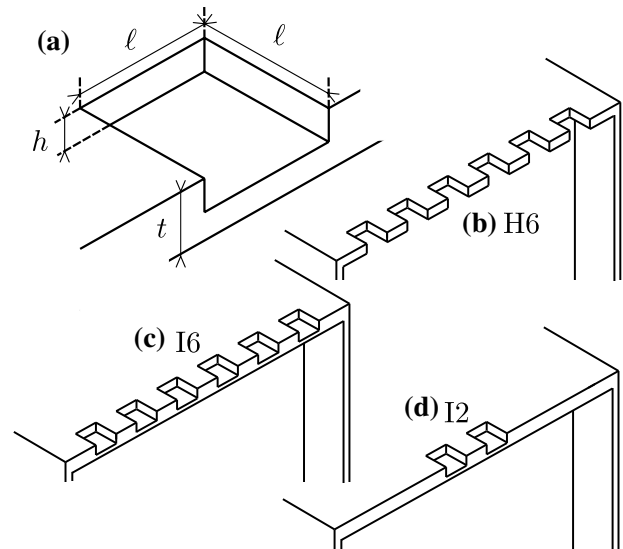


Fig. 3 Top spoiler designs. Basic pattern **a**, spoiler with through-holes **b** and imprints **c**, **d**, see text for dimensions

(of depth h as shown in Fig. 3a for the remainder of the paper. The only configuration with through-holes (H6) is shown in Fig. 3b with $\ell = 25$ mm, $t = 6$ mm, the two other configurations in Fig. 3c, d have identical basic imprints with $h = 6$ mm, $\ell = 25$ mm, $t = 9$ mm and the same pattern repetition as H6 for I6, and only 2 central imprints for I2.

2.3 Pressure and aerodynamic force measurements

Surface pressure measurements are performed using a 64-channel ESP-DTC pressure scanner (with a range of ± 1 kPa) linked to 1 mm diameter pressure tapings by 80 cm-long vinyl tubing. Pressure signals are sampled at 200 Hz. The pressure tap locations at the base are depicted in Fig. 2c. For each pressure tap i , we define a local pressure coefficient:

$$c_{p_i} = \frac{p_i - p_\infty}{\frac{1}{2} \rho U_\infty^2} \tag{1}$$

where p_i is the measured pressure whereas p_∞ is the static pressure measured in the wind tunnel and ρ is the air density.

The instantaneous base suction coefficient c_b is computed as :

$$c_b = -\frac{1}{HW} \iint_{\text{base}} c_p ds. \tag{2}$$

The pressure coefficient is first interpolated over the base from the 45 pressure taps and then integrated. The mean base suction C_b is positive and has to be minimized to reduce the drag of the body. The accuracy on the mean value of C_b is ± 0.001 corresponding to relative uncertainties lower than 0.5%.

Finally, we define the dimensionless components of the pressure coefficient gradient g_y and g_z following the strategies previously used in Grandemange et al. (2013a) in the subsequent equations where indices refer to the taps of Fig. 2c:

$$g_y = \frac{H}{2} \left[\frac{c_{p_{11}} - c_{p_{15}}}{y_{11} - y_{15}} + \frac{c_{p_{12}} - c_{p_{14}}}{y_{12} - y_{14}} \right] \tag{3}$$

and:

$$g_z = \frac{H}{2} \left[\frac{c_{p_3} - c_{p_{23}}}{z_3 - z_{23}} + \frac{c_{p_8} - c_{p_{18}}}{z_8 - z_{18}} \right] \tag{4}$$

The model is mounted on a six-component aerodynamic balance (9129AA Kistler piezoelectric sensors and 5080A charge amplifier), thus providing the 3 components of the mean aerodynamic force \mathbf{F} . The total measurement uncertainty is below 0.6% of the full-scale range, which represents less than 1% uncertainty in the mean drag force F_x for instance.

Force coefficients of drag C_x and lift C_z are defined as follows :

$$C_x = \frac{F_x}{\frac{1}{2} \rho U_\infty^2 HW} \tag{5}$$

$$C_z = \frac{F_z}{\frac{1}{2} \rho U_\infty^2 HW} \tag{6}$$

Measurements of both force and pressure are conducted for 3 minutes duration. No filtering is applied to the data. Measurements are only performed when steady conditions are reached in the tunnel.

2.4 Velocity measurements

Velocity fields in the near wake are measured with a stereoscopic Particle Image Velocimetry (PIV) system. It consists of a Quantel EverGreen 2 × 200 mJ laser of wavelength $\lambda = 532$ nm and two LaVision Imager LX 16 Mpx cameras. The thickness of the laser sheet is approximately 0.01H. The seeding of the flow is introduced downstream of the raised floor and recirculates through the tunnel loop. Particles with

a diameter of 1µm are generated by atomization of mineral oil. Velocity fields are obtained in 2 cross-flow planes, the first at $x = 0.5H$ and the second at $x = H$ downstream the base of the body.

For each cases, 1200 pairs of images are captured at a sample rate of 4Hz, which is satisfactory for statistical convergence of first and second order statistics. Image pairs are processed using DaVis 10.1 software with a final interrogation window of 32 × 32 pixels with an overlap of 50% yielding to a spatial resolution of 0.012H for the velocity field. The width (resp. height) of the PIV field is 1.8H (resp. 1.2H). With a time duration between the laser pulses of 35µs, the maximum uncertainty on the instantaneous velocity fields considering an absolute displacement error of 0.1 pixels is estimated to be of the order of 0.01U_∞. All the PIV measurements have been carried out independently to pressure and aerodynamic force measurements.

3 Results and discussion

In the following, upper case letters *A* stand for time-averaged value of $a(t)$ while primes denote the fluctuating value, $a'(t) = a(t) - A$ and A' is its standard deviation. Usual dimensional variables of space and velocity such as u, x are made non-dimensional using U_∞, H and marked with an asterisk $u^* = u/U_\infty, x^* = x/H$ for the remainder of the paper.

3.1 Impact of the cavity wall designs on the wake balance

Table 1 shows the mean aerodynamic force and base suction for all design configurations. We also show the case without the cavity, corresponding to the Ahmed body (A). As said above, both the low drag and base suction of the reference model (R) compared to that of the Ahmed body (A) are due to the base cavity effect as expected by the study of Evrard et al. (2016). Some of the drag reductions observed in Table 1 falls below the uncertainty of 1% specified in § 2.3 that could be critical for conclusions. Nevertheless, for these cases of weak drag change, the base suction measuring directly the wake contribution to the drag always confirms the trend on the drag.

Table 1 Aerodynamic forces and base suction coefficient for the different rear designs. Variations with respect to the reference design (R) are denoted Δ

Rear design	C_b	ΔC_b	$\Delta C_b(\%)$	C_x	ΔC_x	$\Delta C_x(\%)$	C_z	$\Delta C_z(\%)$
Squareback Ahmed body (A)	0.187	+0.026	+16.15	0.249	+0.022	+9.7	-0.160	+34
Reference (R)	0.161	-	-	0.227	-	-	-0.244	-
6 Holes (H6)	0.159	-0.002	-1.24	0.225	-0.002	-0.9	-0.241	+1.2
6 Imprints (I6)	0.157	-0.004	-2.48	0.227	0	0	-0.201	+17.5
2 Central imprints (I2)	0.147	-0.014	-8.69	0.221	-0.006	-2.7	-0.219	+10.1

The more negative lift of the reference model (R) in Table 1 is attributed to the 5° angle of the bottom cavity wall, responsible for a low pressure at the high curvature at the junction between the 5° cavity wall and the main body. By looking at the effect of the different designs, we can see that a substantial lowest drag is obtained for the 2 central imprints of the I2 configuration, while both homogeneous configurations H6 and I6 produce either small or almost no drag reduction. It can be observed for the I2 configuration where the base suction and drag variation are significantly larger than their measurements uncertainty, that the drag variation ΔC_x is about half the suction variation ΔC_b . Since C_b is a direct contributor to the drag coefficient C_x , it is likely that the top wall design produces a detrimental pressure drag of about $\Delta C_x - \Delta C_b = +0.008$.

The imprint designs I6 and I2 are clearly associated with lift increases on the contrary to the holes design H6. The imprint design must then produce a low pressure on the top cavity wall. It is likely to be related to a flow curvature introduced by the separation at the leading edge of the imprint and its reattachment before the trailing edge. This is consistent with the backward facing step flows of height h , known to reattach at a distance of $4.5h$ at a Reynolds number $\frac{U_\infty h}{\nu} \approx 6000$ (Hudy et al. 2007). Thus in our case, the step dimension $\ell = 25 \text{ mm} \approx 4.5h = 27\text{mm}$ can possibly promote a reattachment at the trailing edge leading to the downwash orientation of the flow similarly to that of an inclined spoiler.

The aim of Fig. 4 is to inform on the global wake property through the variance of the base pressure coefficient gradient components. A wake with a large variance modulus shows a large and permanent degree of asymmetry. The Ahmed body (A) is known to be subjected to a steady y -instability (Grandemange et al. 2012), translating into a large permanent asymmetry in the y -direction as can be seen in Fig. 4. As reported by Grandemange et al. (2013a), the corresponding joint probability of both gradient components in Fig. 5a

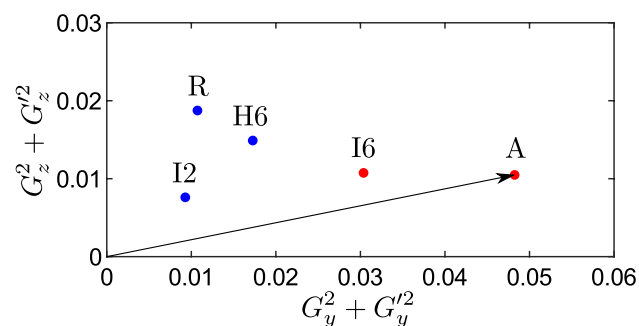


Fig. 4 Variance of the vertical pressure gradient component as a function of the variance of the horizontal pressure gradient component for the 5 rear designs of Table 1. Red points indicate bistable wake dynamics. The arrow indicates the modulus of the base pressure variance for the squareback Ahmed body (A)

displays two most probable states (N and P) from which the wake randomly switches leading to the bistable dynamics.

In Fig. 4, the rear cavity and the 5° angle bottom cavity wall of the reference design (R) have considerably attenuated the variance in the y -direction and increased the gradient variance in the vertical direction. The wake is not bistable anymore as shown in Fig. 5b and the large vertical variance is related to the positive most probable vertical gradient likely to be produced by the 5° angle at the bottom cavity wall.

With the homogeneous imprint design I6, acting similarly to a top inclined cavity wall, the wake that was vertically deviated in the R configuration is re-oriented towards slightly negative value of the most probable vertical gradient (Fig. 5c) thus reducing the vertical variance in Fig. 4. However, the bistability reappears with the I6 design producing a large asymmetry in the y -direction. The wake asymmetry that was mainly vertical in the R configuration is now almost horizontal indicating a global rotation of $\pi/2$ of the wake.

For the holes design H6, it is observed that this top cavity wall does not produce the efficient wake reorientation of the I6 design, leading to a smaller reduction of the vertical variance and smaller increase of the horizontal variance than I6.

Surprisingly, the I2 design achieves a minimal variance in both directions (Fig. 4) with zeros as most probable

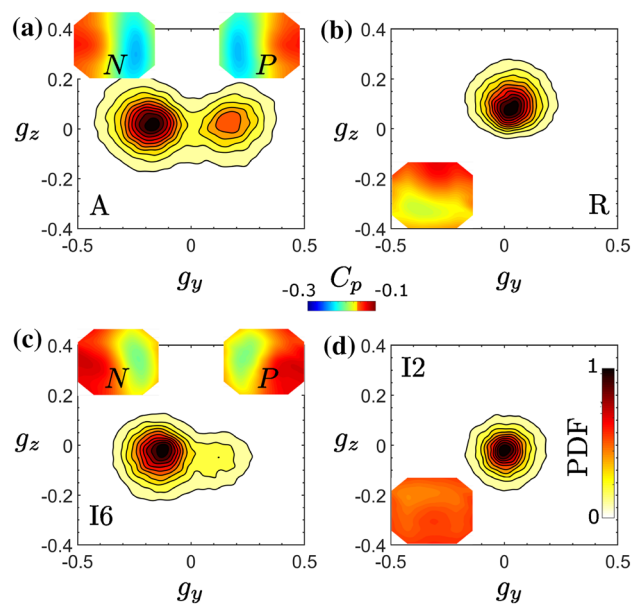


Fig. 5 Joint probability density function $PDF(g_y, g_z)$, normalized by their maximum, of the two pressure gradient components for : **a** squareback body (A), **b** reference case (R), **c** homogeneous imprints (I6) and **d** the central imprints (I2). The mean pressure coefficient distributions, $C_p(y, z)$ are shown as inlet. For the bistable cases observed in **a** and **c**, the C_p distribution at the base is conditionally averaged by $g_y > 0$ to obtain the P state distribution and by $g_y < 0$ to obtain the N state distribution

components of the pressure gradient (Fig. 5d). The wake of this lower drag configuration associated with the lowest wake asymmetry is studied in detail in the next sections together with the R and the I6 configurations.

3.2 Base pressure gradient and base suction correlation

The joint PDFs of the base suction c_b and the horizontal pressure gradient g_y are shown for the three configurations R, I6 and I2 in Fig. 6. The two configurations R and I2 (Fig. 6a and c) look very similar except from the vertical shift due to the low drag configuration of I2 as reported by the mean base suction values given in Table 1. Interestingly, the low mean value of base suction in I2 is also explored during the bistable dynamics of the I6 configuration as can be seen in Fig. 6b. As first reported by Evrard et al. (2016), the passage of the wake at zero horizontal gradient ($g_y = 0$) is associated with low base suction. This so-called transitional state is unstable and corresponds to a symmetric wake. This symmetric wake that has been characterized by Haffner et al. (2020) for an Ahmed body could correspond to the wake when it passes across the zero horizontal gradient in the I2 configuration of Fig. 6b. The subsequent interpretation is that the I2 design suppresses the steady instability present with the I6 design by keeping the wake symmetric with low asymmetry in both directions.

The frequency content of the gradients fluctuation are analysed in Fig. 7 that displays the power spectrum density as a function of the dimensionless frequency, $f^* = f \frac{H}{U_\infty}$. The bistable dynamics is responsible for the power law at low frequency ($f^* < 0.02$) with an approximate exponent of -2 observable in Fig. 7a. It is also in this low frequency range that most of the modifications induced by the cavity wall design occurs in both gradient components. The stabilization

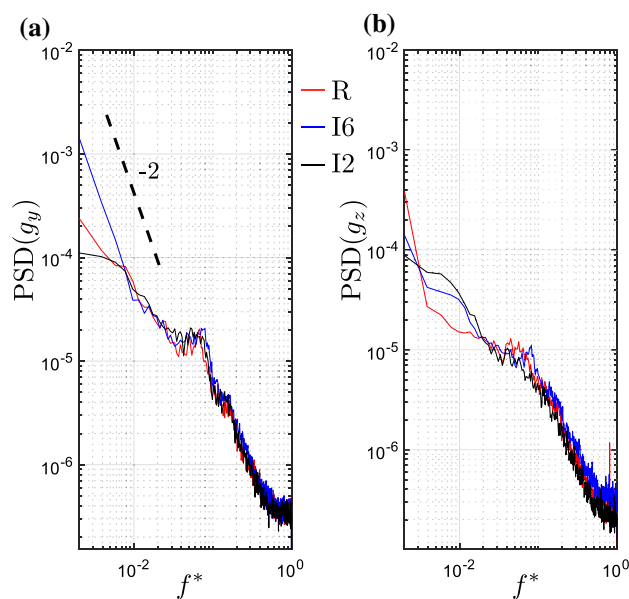


Fig. 7 Power spectral density $PSD(g_y)$ **a** and $PSD(g_z)$ **b** of the two pressure gradient components for : (red) reference case (R), (blue) homogeneous imprints (I6) and (black) the central imprints (I2)

towards a symmetric wake with the I2 design is supported by the similitude of the two PSDs indicating a similar dynamics in both directions.

3.3 Wake velocity fields analysis

We now focus on the wake analysis based on the PIV measurements, particularly on the stabilized (I2) and the reference (R) wake. Mean wake characteristics are shown in two cross-flow planes; at $x^* = 0.5$ in Fig. 8 and $x^* = 1$ in Fig. 9. For each figure, the first column represents the mean streamwise velocity component U^* showing the wake momentum deficit, the second column shows the mean streamwise vorticity component Ω_x to identify longitudinal vortex structures

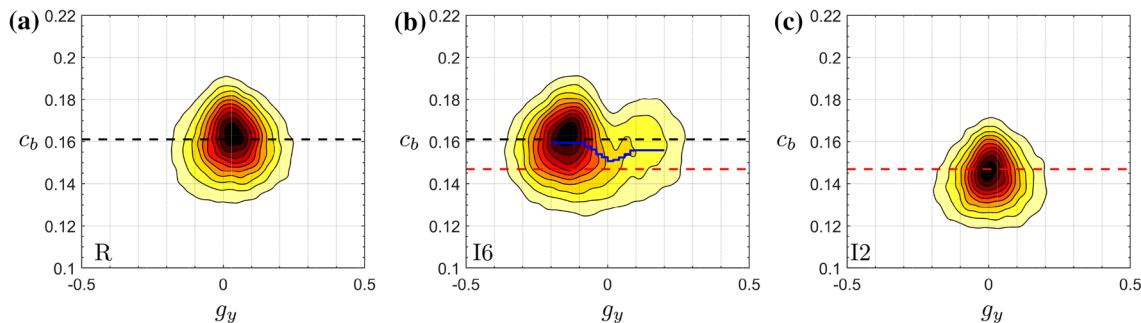


Fig. 6 Joint probability density function $PDF(g_y, c_b)$, normalized by their maximum, of the base suction coefficient and the horizontal pressure gradient for : **a** reference case (R), **b** homogeneous imprints (I6) and **c** the central imprints (I2). Black (resp. red)-dashed line

show the mean base suction C_b for the R configuration (resp. I2 configuration). The blue line in **b** shows the conditional averaging of c_b by the horizontal gradient g_y

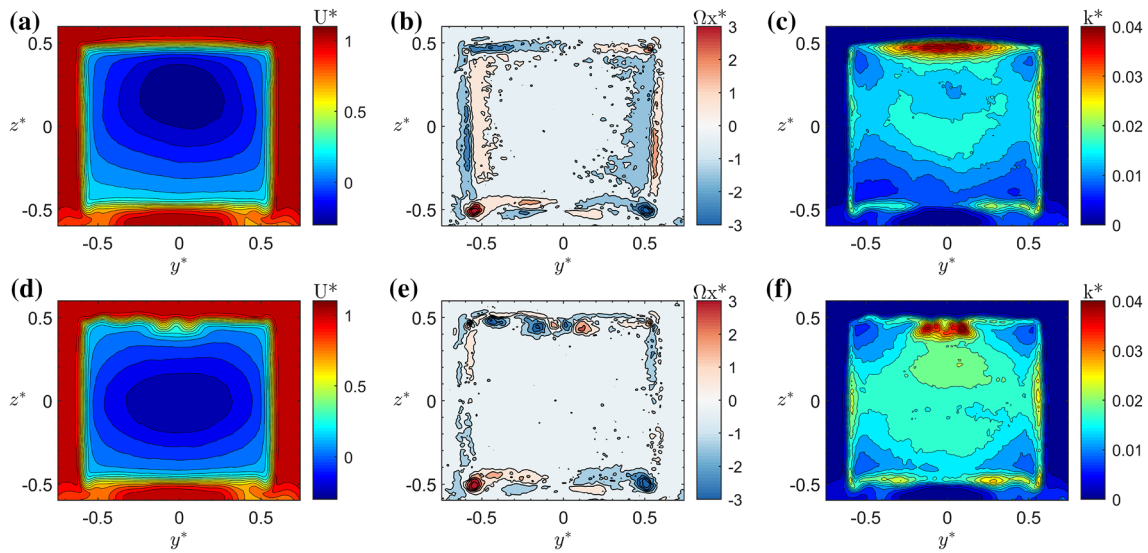


Fig. 8 Mean wake characteristics at $x^* = 0.5$ for the reference (R) wake (top row) and the stabilized (I2) wake (bottom row). Longitudinal velocity **a, d**, mean streamwise vorticity **b, e** and mean turbulent kinetic energy **c, f**. In **b, e**, a clockwise rotation is negative (blue) vorticity and counterclockwise (red) vorticity

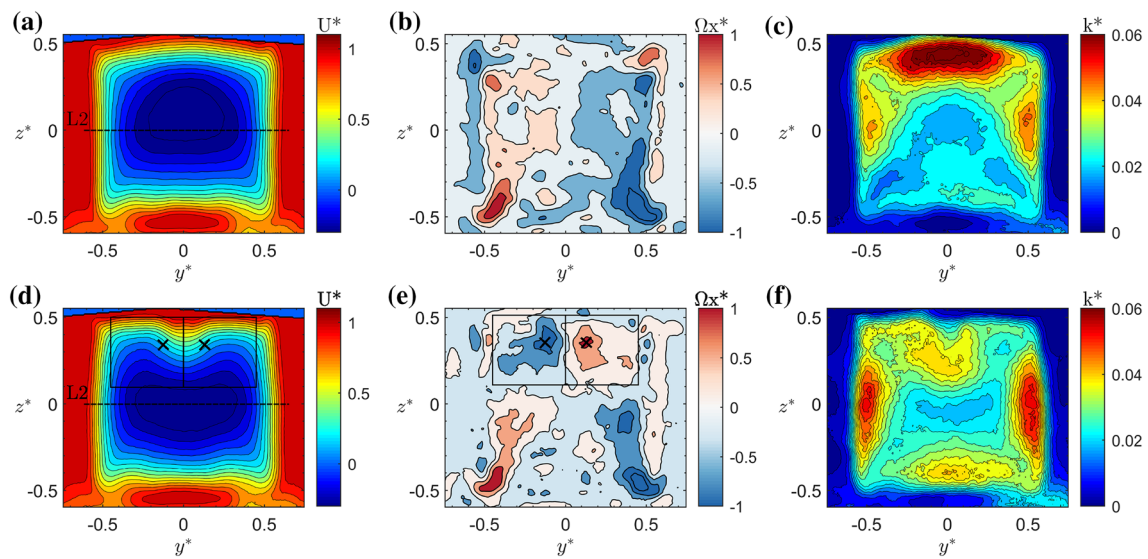


Fig. 9 Mean wake characteristics at $x^* = 1$ for the reference (R) wake (top row) and the stabilized (I2) wake (bottom row). Longitudinal velocity **a, d**, mean streamwise vorticity **b, e** and mean turbulent kinetic energy **c, f**. In **b, e**, a clockwise rotation is negative (blue) vorticity and counterclockwise (red) vorticity. In **e**, square boxes are contours used to calculate the vortex circulation, and crosses indicate their centre

and the third column shows the turbulent kinetic energy k^* to identify the most fluctuating regions of the wake. The top row corresponds to the reference R wake and the second to the stabilized I2 wake.

Comparing the mean streamwise velocity fields, it is clear that the stabilized wake momentum deficit region is far better centered on the rectangular base than that of the reference wake (see Figs. 8a, d and 9a, d). Except from the

flow disturbances due to the imprints observable in the top shear layer in Fig. 8d, the stabilized wake at $x^* = 0.5$ has the same reflectional symmetries as the base with respect to the $y^* = 0$ and $z^* = 0$ axis. The flow disturbance of the 2 central imprints observed in the streamwise velocity are revealed to be two pairs of longitudinal counter-rotating vortices in Fig. 8e, that are totally absent in the reference wake in Fig. 8b. The two vortices at both ends of the two

pairs grow downstream as can be seen at $x^* = 1$, inside the 2 square boxes drawn in Fig. 9e. The 2 central vortices of the 2 pairs have completely disappeared. The turbulent kinetic energy of the reference wake in Fig. 8c and Fig. 9c exhibits a dominant $m = 1$ azimuthal distribution, with maximum fluctuations located at the top of the wake. Together with the vertical positive base gradient observed in Fig. 4b, the wake of the R configuration is then similar to that described by the sketch in Fig. 1b. It is replaced by a dominant $m = 2$ distribution in the stabilized wake in Figs. 8f and 9f.

It is likely that the stabilization of the wake is the consequence of the formation of the two longitudinal vortices inside the recirculating area evidenced in Fig. 9e, that might shift downwards the momentum deficit of the reference wake by their vertical-induced velocity together with reducing significantly the turbulent fluctuation in the upper shear layer. The rotation flow they induce in the recirculating area is also consistent with the observation of the increased width of the wake around $z^* = 0$ and of its shrinkage around $z^* = 0.5$ in Fig. 8c compared to Fig. 8f. This flow distortion interpretation of the recirculating area is emphasized in Fig. 10 showing the difference of the velocity fields between the stabilized and reference wake for the vertical W and the horizontal component V in Fig. 10a and b, respectively. While Fig. 10a clearly displays the downwash effect with the large negative velocity induced by the vortex pair, their quadrupole structure in Fig. 10b for the horizontal velocity

component produces both the wake enlargement around $z^* = 0$ and the shrinkage around $z^* = 0.5$. These velocity differences are now compared to a simple model of two point vortices whose induced velocity is computed from the Biot and Savart law (Saffman 1992). The two point vortices are located at the cross symbols displayed in Fig. 9e and having the circulation computed from the sum of the vorticity contained inside each of the square boxes also displayed in Fig. 9e. The obtained circulations are respectively $\Gamma_+^* = +0.46$ and $\Gamma_-^* = -0.44$ for the right and left vortex. Fig. 10c, d compares the velocity profiles along the vertical line displayed in Fig. 10a for W in Fig. 10c and along the horizontal line displayed in Fig. 10b for V in Fig. 10d. A satisfactorily match in amplitude is obtained for the vertical velocity component (Fig. 10c). Thus confirming that the downwash flow in the recirculating region observed with the design I2 is dominated by the pair of vortices. However, the 2 point vortices produce weak horizontal velocity at mid height of the base.

A final remark is that the central pair of vortices that has disappeared between the 2 measurement planes at $x^* = 0.5$ (Fig. 8e) and $x^* = 1$ (Fig. 9e) is useless for the stabilisation mechanism and in addition, that this pair is possibly associated with extra drag. We verified this during a last test involving base pressure measurements only and a single large imprint design LI1 having a width of 111mm, equal to one third of the width of the horizontal cavity wall, and a depth of 6mm (Fig. 11a). Without checking with PIV measurements, we can argue that such a geometry only creates the 2 relevant longitudinal vortices needed for the stabilisation mechanism discussed above. Indeed, for this new design (LI1) the wake balance assessed with the joint statistics of the pressure gradient components in Fig. 11a evidencing low variance in both directions is clearly achieved, similarly to the I2 design in Fig. 4d. Both the low base suction and the low gradient variance are consistent with a stabilized wake. The corresponding drag reported in Table 2 is even lower than that of the I2 design.

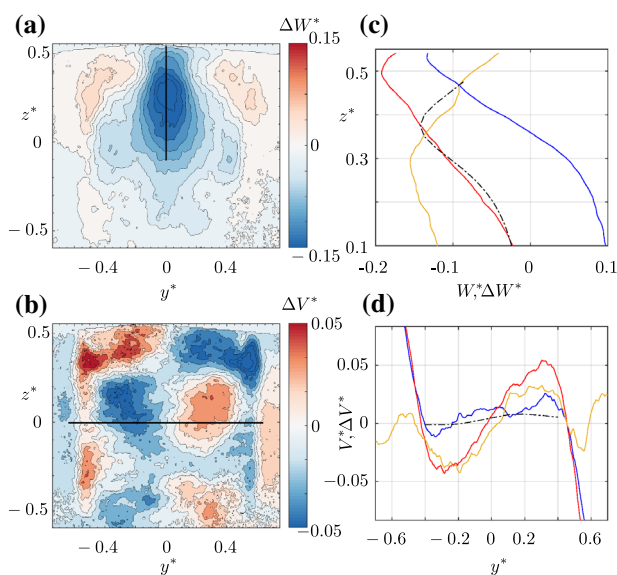


Fig. 10 Differences of the vertical ΔW **a** and horizontal ΔV **b** velocity field between the central imprints (I2) and reference (R) designs in the plane $x^* = 1$. Vertical **c** and horizontal **d** velocity profiles along the black line displayed in **a** and **b** respectively of the (I2, red line) and (R, blue line) designs. The velocity difference is displayed as orange-dashed lines. The two point vortices model (see text) is shown as dashed black lines in (**c**, **d**)

4 Conclusion

The present investigation leads to the following conclusions :

Table 2 Aerodynamic forces and base suction coefficient for the different top cavity wall designs

Configuration	C_b	C_x	C_z
I2	0.147	0.221	-0.219
Large imprint (LI1)	0.144	0.220	-0.212

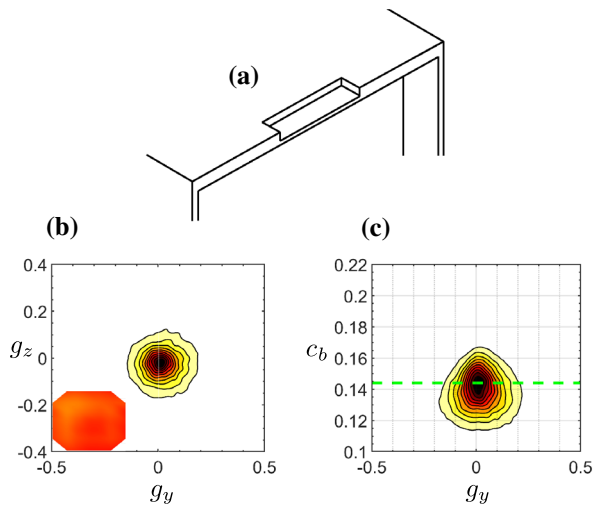


Fig. 11 Central large imprint experiment. Spoiler design LII (a), joint probability density functions $PDF(g_y, g_z)$ (b) and $PDF(g_y, c_b)$ (c) normalized by their maximum with the same colorbar as in Fig. 4. The mean pressure coefficient distribution, $C_p(y, z)$ is shown as inlet in (b) with the same colorbar as in Fig. 4

- The variance of the base pressure gradient components is useful to characterize the wake balance in both lateral directions. For the Ahmed body the smaller the variance, the better the wake is balanced. It may be of practical importance at the industrial scale for an alternative easy and fast wake balance diagnose compared to wake flow survey using tomographic techniques based on multi-holes pressure probes or PIV measurements. During the aerodynamic development of their SUV, De Boer et al. (2022) pointed out the relationship between the vertical base pressure gradient orientation, the wake orientation and the base drag when different top spoiler designs were tested.
- Imprint spoilers influence the wake in a similar way as an inclined spoiler and can be used to balance the wake. In addition, each longitudinal edge of the imprint produces a longitudinal vortex that penetrates the recirculation area.
- A large central imprint produces a pair of counter-rotating vortices inside the recirculating area able to symmetrize the wake initially in a strong $m=1$ azimuthal wake dominated mode towards a $m=2$ wake dominated mode respecting the symmetry of the rectangular base in both lateral and vertical directions.

This particular design that balances the wake is therefore also stabilizing the wake steady instability to achieve a better drag reduction. The longitudinal vorticity introduced by the imprint has a key role for the academic Ahmed geometry studied here. On real car geometries, introducing specific tri-dimensionnal spoiler shapes may offer interesting design and

engineering perspectives in order to achieve drag reduction and to increase the autonomy of vehicles, a crucial endeavour particularly with electric cars.

Acknowledgements The authors would like to warmly thank J.-M. Breux for invaluable support during the experiments, as well as F. Paillé, P. Braud and R. Bellanger for assistance with the aerodynamic balance and the PIV set-up. We are indebted to Stellantis (OpenLab Fluidics@Poitiers) and to the CPER Feder programme Transport for financial support.

Author Contributions G.B. and T.D. produces the results. All authors analysed the results. T.D. prepared all figures and a first draft. O.C. and J.B. wrote the final version. All authors reviewed the manuscript.

Funding The work has been funded by Stellantis (OpenLab Fluidics@Poitiers) and the CPER Feder programme Transport.

Availability of data and materials on request to the authors

Declarations

Ethical Approval not applicable

Conflict of interest The authors declare that they have no conflict of interest

Open Access This article is licensed under a Creative Commons Attribution 4.0 International License, which permits use, sharing, adaptation, distribution and reproduction in any medium or format, as long as you give appropriate credit to the original author(s) and the source, provide a link to the Creative Commons licence, and indicate if changes were made. The images or other third party material in this article are included in the article's Creative Commons licence, unless indicated otherwise in a credit line to the material. If material is not included in the article's Creative Commons licence and your intended use is not permitted by statutory regulation or exceeds the permitted use, you will need to obtain permission directly from the copyright holder. To view a copy of this licence, visit <http://creativecommons.org/licenses/by/4.0/>.

References

- Bao D, Borée J, Haffner Y, Sicot C (2022) Near wake interactions and drag increase regimes for a square-back bluff body. *J Fluid Mech* 936:A2. <https://doi.org/10.1017/jfm.2022.28>
- Barros D, Borée J, Cadot O, Spohn A, Noack BR (2017) Forcing symmetry exchanges and flow reversals in turbulent wakes. *Journal of Fluid Mechanics* 829:R
- Bonnayon G, Cadot O (2019) Boat-tail effects on the global wake dynamics of a flat-backed body with rectangular section. *J Fluids Structures* 89:61–71
- Bonnayon G, Cadot O, Évrard A, Herbert V, Parpais S, Vigneron R, Détery J (2017) On multistabilities of real car's wake. *J Wind Eng Indus Aerodyn* 164:22–33
- Brackston RD, García De La Cruz J, Wynn A, Rigas G, Morrison JF (2016) Stochastic modelling and feedback control of bistability in a turbulent bluff body wake. *J Fluid Mech* 802:726–749
- Chaligné S, Turner R, Gaylard A (2017) The aerodynamics development of the new land rover discovery. In: Wiedemann J (ed) *Progress in vehicle aerodynamics and thermal management*. Springer International Publishing, New York, pp 1–20

- Dalla Longa L, Evstafyeva O, Morgans A (2019) Simulations of the bi-modal wake past three-dimensional blunt bluff bodies. *J Fluid Mech* 866:791–809
- De Boer M, Gaylard AP, Parmar B (2022) The aerodynamic development of the new range rover evoke. SAE Technical Papers 2022-01-0890
- Evrard A, Cadot O, Herbert V, Ricot D, Vigneron R, Détery J (2016) Fluid force and symmetry breaking modes of a 3D bluff body with a base cavity. *J Fluids Struct* 61:99–114
- Evstafyeva O, Morgans AS, Dalla Longa L (2017) Simulation and feedback control of the ahmed body flow exhibiting symmetry breaking behaviour. *J Fluid Mech* 817:R
- Fan Y, Xia C, Chu S, Yang Z, Cadot O (2020) Experimental and numerical analysis of the bi-stable turbulent wake of a rectangular flat-backed bluff body. *Phys Fluids* 32(10):105111
- Fan Y, Parezanović V, Cadot O (2022) Wake transitions and steady z -instability of an ahmed body in varying flow conditions. *J Fluid Mech* 942:A22. <https://doi.org/10.1017/jfm.2022.382>
- Grandemange M, Gohlke M, Cadot O (2012) Reflectional symmetry breaking of the separated flow over three-dimensional bluff bodies. *Phys Rev E* 86:035302
- Grandemange M, Gohlke M, Cadot O (2013) Bi-stability in the turbulent wake past parallelepiped bodies with various aspect ratios and wall effects. *Phys Fluids* 25:95–103
- Grandemange M, Gohlke M, Cadot O (2013) Turbulent wake past a three-dimensional blunt body. Part I. Global modes and bi-stability. *J Fluid Mech* 722:51–84
- Grandemange M, Mary A, Gohlke M, Cadot O (2013) Effect on drag of the flow orientation at the base separation of a simplified blunt road vehicle. *Exp Fluids* 54(5):1–10
- Haffner Y, Borée J, Spohn A, Castelain T (2020) Mechanics of bluff body drag reduction during transient near-wake reversals. *J Fluid Mech* 894:A14
- Haffner Y, Castelain T, Borée J, Spohn A (2021) Manipulation of three-dimensional asymmetries of a turbulent wake for drag reduction. *J Fluid Mech* 912
- Han T, Hammond D, Sagi C (1992) Optimization of bluff body for minimum drag in ground proximity. *AIAA J* 30(4):882–889
- Hsu EC, Pastur L, Cadot O, Parezanović V (2021) A fundamental link between steady asymmetry and separation length in the wake of a 3d square-back body. *Exp Fluids* 62(5):1–5
- Hudy LM, Naguib A, Humphreys WM (2007) Stochastic estimation of a separated-flow field using wall-pressure-array measurements. *Phys Fluids* 19(2):024103
- Li R, Barros D, Borée J, Cadot O, Noack BR, Cordier L (2016) Feedback control of bimodal wake dynamics. *Exp Fluids* 57(10):158
- Li R, Jacques B, Noack B, Cordier L, Harnambat F (2019) Drag reduction mechanisms of a car model at moderate yaw by bi-frequency forcing. *Phys Rev Fluids* 4:034604
- Littlewood R, Passmore M (2010) The optimization of roof trailing edge geometry of a simple squareback. SAE Technical Paper Series 2010-01-0510
- Luckhurst S, Varney M, Xia H, Passmore M, Gaylard A (2019) Computational investigation into the sensitivity of a simplified vehicle wake to small base geometry changes. *J Wind Eng Indus Aerodyn* 185:1–15. <https://doi.org/10.1016/j.jweia.2018.12.010>
- Pavia G, Passmore M (2018) Characterisation of wake Bi-stability for a square-back geometry with rotating wheels. In: Wiedemann J (ed) *Progress in vehicle aerodynamics and thermal management*. Springer International Publishing, New York, pp 93–109
- Pavia G, Passmore M, Gaylard A (2016) Influence of short rear end tapers on the unsteady base pressure of a simplified ground vehicle. SAE Technical Paper Series
- Pavia G, Passmore M, Sardu C (2018) Evolution of the bi-stable wake of a square-back automotive shape. *Exp Fluids* 59(1):20
- Pavia G, Passmore MA, Varney M, Hodgson G (2020) Salient three-dimensional features of the turbulent wake of a simplified square-back vehicle. *J Fluid Mech* 888:A33
- Perry A, Pavia G, Passmore M (2016) Influence of short rear end tapers on the wake of a simplified square-back vehicle: wake topology and rear drag. *Exp Fluids* 57(11):169
- Podvin B, Pellerin S, Fraigneau Y, Bonnavion G, Cadot O (2021) Low-order modelling of the wake dynamics of an Ahmed body. *J Fluid Mech* 927:R6
- Saffman P (1992) *Vortex dynamics*. Cambridge University Press, Cambridge, MA
- Schmidt HJ, Woszidlo R, Nayeri CN, Paschereit CO (2018) The effect of flow control on the wake dynamics of a rectangular bluff body in ground proximity. *Exp Fluids* 59(6):107
- Urquhart M, Sebben S (2022) Optimisation of trailing edge flaps on the base cavity of a vehicle for improved performance at yaw. *Flow Turb Combust*, p 109
- Urquhart M, Varney M, Sebben S, Passmore M (2020) Aerodynamic drag improvements on a square-back vehicle at yaw using a tapered cavity and asymmetric flaps. *Int J Heat Fluid Flow* 86:108737
- Urquhart M, Varney M, Sebben S, Passmore M (2021) Drag reduction mechanisms on a generic square-back vehicle using an optimised yaw-insensitive base cavity. *Exp Fluids* 62(12):1–21
- Volpe R, Devinant P, Kourta A (2015) Experimental characterization of the unsteady natural wake of the full-scale square back Ahmed body: flow bi-stability and spectral analysis. *Exp Fluids* 56(5):1–22
- Wong DM, Mair W (1983) Boat-tailed afterbodies of square section as drag-reduction devices. *J Wind Eng Indus Aerodyn* 12(2):229–235. [https://doi.org/10.1016/0167-6105\(83\)90071-5](https://doi.org/10.1016/0167-6105(83)90071-5)

Publisher's Note Springer Nature remains neutral with regard to jurisdictional claims in published maps and institutional affiliations.